Raman spectroscopy evidence for dimerization and Mott collapse in α-$RuCl_3$ under pressures

Gaomin Li,[1,2] Xiaobin Chen,[3] Yuan Gan,[4] Fenglei Li,[4] Mingqi Yan,[4] Fan Ye,[4] Shenghai Pei,[2] Yujun Zhang,[2] Le Wang,[5] Huimin Su,[4] Junfeng Dai,[4] Yuanzhen Chen,[2,6] Youguo Shi,[5] XinWei Wang,[1] Liyuan Zhang,[4] Shanmin Wang,[4] Dapeng Yu,[2,6] Fei Ye,[2,*] Jia-Wei Mei,[2,†] and Mingyuan Huang[2,6,‡]

[1]*School of Advanced Materials, Shenzhen Graduate School Peking University, Shenzhen 518055, China*

[2]*Shenzhen Institute for Quantum Science and Engineering, and Department of Physics, Southern University of Science and Technology, Shenzhen 518055, China*

[3]*School of Science, Harbin Institute of Technology, Shenzhen 518055, China*

[4]*Department of Physics, Southern University of Science and Technology, Shenzhen 518055, China*

[5]*Institute of Physics, Chinese Academy of Sciences, Beijing 100190, China*

[6]*Shenzhen Key Laboratory of Quantum Science and Engineering, Shenzhen 518055, China*

(Received 16 August 2018; published 8 February 2019)

We perform Raman spectroscopy studies on α-$RuCl_3$ at room temperature to investigate its phase transitions of magnetism and structure under pressure. The Raman measurements resolve two critical pressures at $p_1 = 1.1$ GPa and $p_2 = 1.7$ GPa with very different structural and magnetic behaviors. With increasing pressure, a stacking order phase transition of α-$RuCl_3$ occurs at p_1, indicated by the new Raman modes. The appearance of infrared active modes in Raman spectrum usually results from the inversion symmetry breaking, which is confirmed by the second harmonic generation measurement. The second transition at p_2 is signaled by the in-plane Ru-Ru bond dimerization accompanied by the Mott collapse and the system becomes a correlated band insulator. Our studies demonstrate the competition among spin-orbit coupling, magnetism, and chemical bondings in Kitaev compounds.

DOI: 10.1103/PhysRevMaterials.3.023601

I. INTRODUCTION

The spin-orbit coupling invigorates new vitality to the intertwining of magnetism and chemical bonds [1–5]. It may generate the bond-dependent Dzyaloshinsky-Moriya and Ising-type interactions [2–4]. The latter one is of current interest, which gives rise to the exactly solvable Kitaev model when implemented on a honeycomb lattice [6–8]. The ground state of Kitaev model [6] belongs to the family of quantum spin liquids, in which the spins do not freeze even at zero temperature [9], but exhibit long-range entanglement [6,10,11] and fractional excitations [12–18]. Recently, Kitaev interactions have been identified in layered honeycomb magnetic materials, such as α-A_2IrO_3 (A=Na, Li) [19–21] and α-$RuCl_3$ [22]. However, due to other non-Kitaev interactions, these materials shows long-range magnetic orders at low temperatures [23–27]. To achieve a real quantum spin liquid state, one needs to suppress the magnetic orders. In α-$RuCl_3$, this can be implemented by applying the in-plane magnetic fields, and the resulting magnetic properties are consistent with theoretical expectations [28–36].

Pressure could also break down the magnetic order in α-$RuCl_3$ [37–40]. Indeed, the magnetic signals disappear above a critical pressure indicating the occurrence of a magnetic phase transition [37–39]. It is worth noting that, during this transition, the charge gap does not change significantly and the system remains in an insulating state [37]. At present, the nature of this transition is unclear, and there is a debate on whether or not this pressure induced phase transition is accompanied by a crystal deformation resulting from the chemical bondings. As reported previously in Ref. [37], the x-ray diffraction (XRD) measurement did not show any structural phase transition up to 150 GPa, and to account for the high pressure nonmagnetic state a new quantum magnetic disordered state was raised. However, a later XRD measurement in Ref. [39] revealed a Ru-Ru bond dimerization of about 0.6 Å above a critical pressure. Furthermore, in Ref. [40], a similar nonmagnetic dimerized scenario was also deduced in the optical measurements. These results are reminiscent of recent high-pressure investigations on the two-dimensional Kitaev material α-Li_2IrO_3 [41] and its three-dimensional polymorph β-Li_2IrO_3 [42]. At high pressures, α-Li_2IrO_3 dimerizes [41], while β-Li_2IrO_3 manifests the coexistence of both the dynamically correlated and the frozen spins without structural deformation [42].

In this paper, we perform Raman scattering measurements on α-$RuCl_3$ to study the nature of the phase transitions under pressures. Since the Raman spectroscopy is capable of simultaneously detecting the phonon and magnetic excitations [43–50], it becomes an exemplary experimental tool to explore the magnetism and chemical bondings of the Kitaev-type compounds [47,51–54]. Our measurements are carried out at room temperature. To further our understanding about the experimental results, we performed first-principles calculation based on an isolated single layer model to

*yef@sustc.edu.cn
†meijw@sustc.edu.cn
‡huangmy@sustc.edu.cn

determine the eigenvectors of the observed Raman modes. By tracking the evolution of the Raman spectra, we identify two characteristic pressures $p_1 = 1.1$ GPa and $p_2 = 1.7$ GPa for structural phase transitions. Around the first critical pressure p_1, new Raman modes appear and the inversion symmetry breaks, which is confirmed by the second harmonic generation (SHG) measurement. The space group of the system changes from the monoclinic $C2/m$ to the trigonal $P3_112$ owing to the variations of the stacking pattern of the α-$RuCl_3$ layers. At the second critical pressure p_2, the in-plane Raman mode of ruthenium atoms softens and splits, indicating the dimerization of the Ru-Ru bonds. Besides the variation of phonon modes, we also observed a sequential change of the Raman susceptibility with increasing pressure as following: it is greatly enhanced first, slightly adjusted at p_1, and sharply decreased after the dimerization at p_2. Thus the Mott collapse occurs at the second critical pressure p_2.

II. EXPERIMENTAL SETUP AND METHODS

High-quality single crystals of α-$RuCl_3$ are grown from commercial $RuCl_3$ powder by chemical vapor transport method. We use the diamond anvil cell to apply hydrostatic pressures on the samples, and calibrate the value of pressures by the shift of the photoluminescence of Ruby. Raman spectrum measurement is conducted using a 633-nm laser in the backscattering configuration with the light polarized in the basal plane. The light is focused down to 3 μm with the power below 1 mW. Two ultranarrow band notch filters are used to suppress the Rayleigh scattering light. The scattering light is dispersed by a Horiba iHR550 spectrometer and detected by a liquid nitrogen cooled CCD detector. The measurement using a 488-nm laser is given in Appendix A for comparison. For the SHG measurement, a 1010-nm pulse laser was focused on the sample and the 505-nm signal was detected.

Density functional calculations were performed using the Vienna *ab initio* simulation package (VASP) within the Perdew-Burke-Ernzerhof generalized gradient approximation (PBEsol-GGA and PBE-GGA). The projector-augmented wave (PAW) potentials were used to describe the atomic potentials with a cutoff energy of 500 eV. The spin-orbit coupling (SOC) was included. The effects due to the localization of the d electrons of the transition metal ions are taken into account using the GGA + U approach with the Coulomb onsite repulsion energy of 1.5 eV on Ru atoms. Sufficient k-point meshes of $7 \times 7 \times 1$ were used for sampling the Brillouin zone. The atomic structures were fully relaxed with symmetry until the Helmann-Feynman forces were less than 0.002 eV/Å. Afterward, the oscillation spectrum of monolayer α-$RuCl_3$ in the antiferromagnetic configuration was obtained using the density functional perturbation theory.

III. EXPERIMENTAL RESULTS OF RAMAN AND IR SPECTRA

Figure 1 displays the evolution of the Raman spectra of α-$RuCl_3$ from ambient pressure to 9.4 GPa. The highest measured pressure is up to 24 GPa and the pressure process is reversible (see Appendix A, Fig. 7). Here, we can identify two characteristic pressures, $p_1 = 1.1$ GPa and $p_2 = 1.7$ GPa,

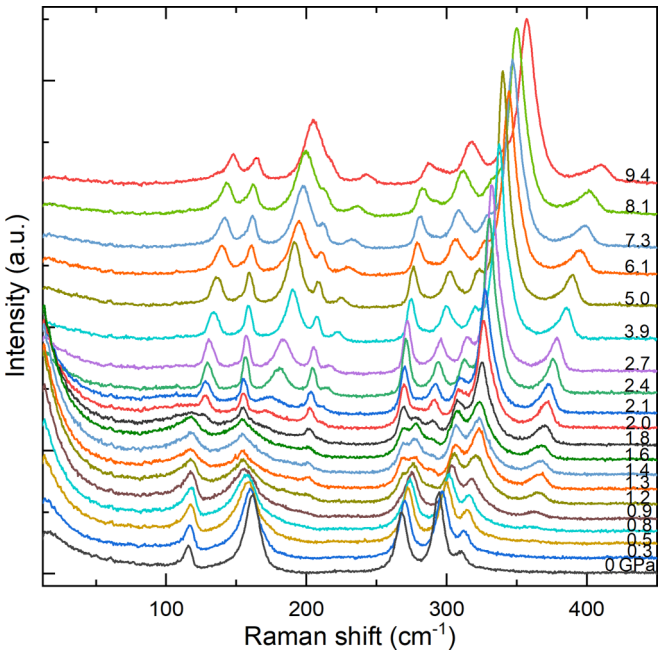

FIG. 1. Evolution of the Raman spectra of α-$RuCl_3$ under different pressures at room temperature.

at which the dramatic change of Raman spectra implies the structural phase transitions. At ambient pressure, five Raman modes are clearly resolved at 116, 161, 268, 294, and 310 cm^{-1}. Besides the phonon Raman modes, we can also observe the Quasielastic scattering below 200 cm^{-1}, which is originated from the magnetic excitations [52,54]. At $p_1 =$ 1.1 GPa, three new Raman modes at 201, 290, and 363 cm^{-1} appear. The original five modes evolve as following. The mode originally at 116 cm^{-1} disappears at $p_2 = 1.7$ GPa, and a new mode splits out at the right side simultaneously. The 161 cm^{-1} mode splits at p_2. For the 268-cm^{-1} mode, a new peak develops at the left side at p_1 and the original one disappears at p_2. No splitting can be resolved for the 294-cm^{-1} mode and the intensity of the 310-cm^{-1} mode experiences a dramatic increase for $p > p_2$. No abrupt change of all Raman peaks is observed from p_2 up to 24 GPa as shown Fig. 7 in the Appendix.

The previous Raman studies showed that the difference of the Raman spectra of different stacking order samples is very small and the interlayer interaction is negligible [54]. To confirm this result, the layer dependence of infrared (IR) and Raman spectra have been investigated. As shown in Fig. 2(a), we performed IR measurement on exfoliated sample down to three layers and no peak shift has been observed. That means the electronic structure of α-$RuCl_3$ is independent of the layer number. In addition, the Raman spectra of the different thickness of α-$RuCl_3$ were also measured, as displayed in Fig. 2(b). It is obvious that the Raman spectra of these five samples are all the same except the intensity. In another word, the Raman spectrum of α-$RuCl_3$ can be understood by an isolated single layer model.

Then, we can assign the Raman modes at ambient pressure according to the D_{3d} point group of the single α-$RuCl_3$ layer. The irreducible representation of atomic displacement

TABLE I. The calculated frequencies of all optical vibrational modes (the frequency unit is cm^{-1}).

	Raman active						IR active					inactive		
Mode	A_{1g}		E_g				A_{2u}		E_u			A_{2g}		A_{1u}
Calc. this work	149	289	111	153	253	279	124	320	156	257	290	140	269	282
Expt. this work	NA	310	116	161	268	294	NA	363 (1.1 GPa)	201 (1.1 GPa)	NA	NA	NA	291 (1.1 GPa)	NA

at the Γ point is $\Gamma_{opt} = 2A_{1g} + 2A_{2g} + 4E_g + A_{1u} + 2A_{2u} + 3E_u$. Among them, Raman active modes are $\Gamma_R = 2A_{1g} + 4E_g$. From the polarization measurement [see Appendix B, Fig. 8(a)] and previous Raman studies [52], the first four modes are assigned as doubly degenerated E_g mode and the last one as A_{1g} mode.

We can determine the eigenvectors of Raman modes with the help of the first-principles calculations and the calculated frequencies of all optical vibrational modes are listed in Table I along with their symmetry. The atomic displacements of five observed Raman-active modes are displayed in Fig. 3(a). For the four E_g modes, the 116-cm^{-1} mode is dominated by the twist of the Ru-Cl-Ru-Cl plane; the 161-cm^{-1} mode is associated with Ru in-plane relative movement; the 268-cm^{-1} mode is related to the Ru-Cl-Ru-Cl plane shearing, and the 294-cm^{-1} mode is the breathing mode of Ru-Cl-Ru-Cl ring. The A_{1g} mode at 310 cm^{-1} can be assigned as the symmetrical breathing mode between the upper and lower chlorine layers. There is actually another A_{1g} mode, corresponding to the relative twist between the upper and lower chlorine triangles, with the calculated frequency about 149 cm^{-1}, which is close to the frequencies of the A_{1g} modes observed in $CrCl_3$ [54] and $FeCl_3$ [55], 142 and 165 cm^{-1}, respectively. Since there is no A_{1g} peak observed in this range for α-$RuCl_3$, we believe that this mode is unresolvable due to its small scattering cross section.

IV. STRUCTURAL AND MAGNETIC PHASE TRANSITIONS UNDER PRESSURES

A. Inversion symmetry breaking at $p_1 = 1.1$ GPa

The main feature at p_1 is the appearance of three new Raman modes at 201, 290, and 363 cm^{-1}. According to the group theory and the first-principles calculations of the single α-$RuCl_3$ layer, we assign the 201-cm^{-1} mode, which splits after p_2, as an IR-active E_u mode, the 290-cm^{-1} mode as an inactive A_{2g} mode, and the 363-cm^{-1} mode, which has the highest frequency, as an IR-active A_{2u} mode and which is related to the asymmetrical layer breathing mode as shown in Fig. 9 in the Appendix.

The appearance of IR-active modes in Raman spectrum indicates the inversion symmetry breaking. To confirm this, the second harmonic generation (SHG) measurement was also performed on pressured samples. As displayed in Fig. 4, no SHG signal was detected before 0.88 GPa, but SHG signal was detected at 1.13 GPa and higher pressure, which is consistent with inversion symmetry breaking at around 1.1 GPa. Since there is no significant change in the original Raman

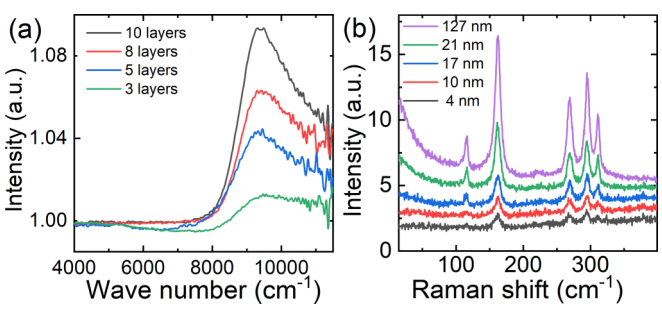

FIG. 2. The layer dependence of IR (a) and Raman (b) spectra of α-$RuCl_3$.

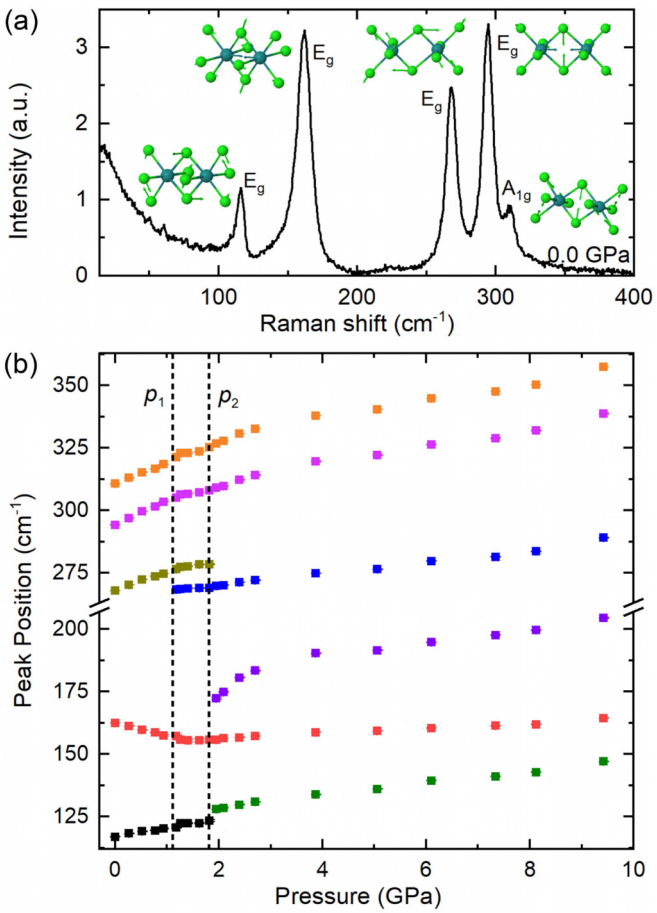

FIG. 3. (a) The Raman spectrum and the corresponding atomic displacements of the five Raman active modes ($4E_g + 1A_{1g}$) in α-$RuCl_3$ under ambient pressure, where only one of the doubly degenerated E_g modes is given. (b) Pressure dependence of the frequencies of the five Raman peaks. $p_1 = 1.1$ GPa and $p_2 = 1.7$ GPa are two critical pressures.

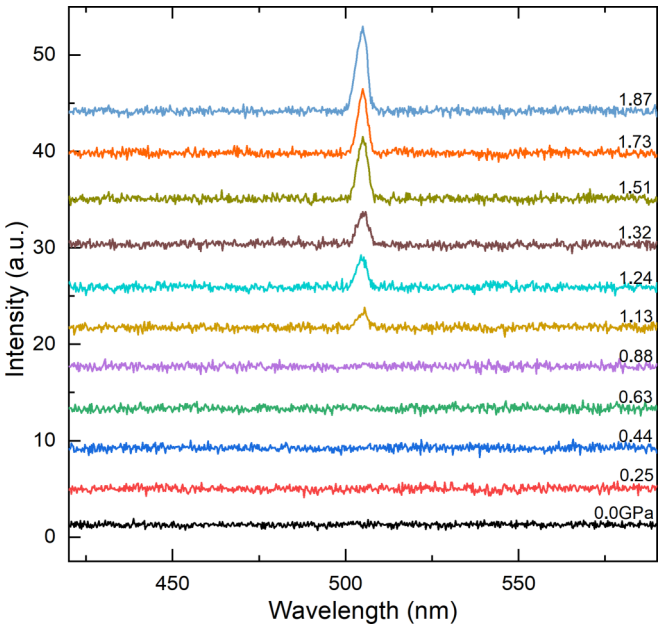

FIG. 4. Second harmonic generation (SHG) of α-$RuCl_3$ under different pressures.

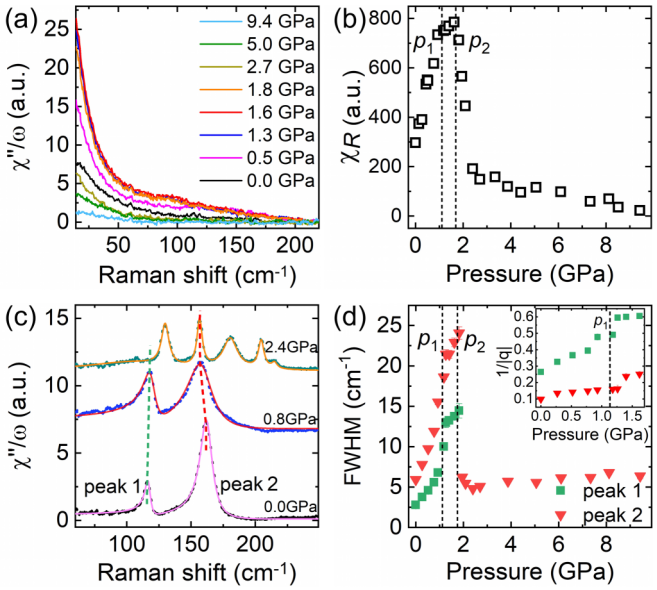

FIG. 5. Pressure dependence of the magnetic Raman conductivity χ''/ω and the magnetic Raman susceptibility χ_R, in (a) and (b), respectively. (c) The phonon Raman spectra (after subtracting the magnetic continuum) for the 116-cm^{-1} mode (peak 1) and the 161-cm^{-1} mode (peak 2) under various pressures. The spectra under 0.0 GPa and 0.8 GPa were fitted by Fano lineshapes. The spectrum under 2.4 GPa was fitted by Lorentz line shape. (d) Pressure dependence of the full width at half maximum (FWHM) and the Fano asymmetry parameter $1/|q|$ (the inset) for the peak 1 and 2. The vertical dash lines in (b) and (d) indicate the critical pressures.

modes, the inversion symmetry breaking is a consequence of the change of stacking pattern of the α-$RuCl_3$ layers.

B. Dimerization transition at $p_2 = 1.7$ GPa

As shown in Fig. 3(b), almost all of the Raman modes show blueshift with the increasing pressure. However, the Ru in-plane mode at 161 cm^{-1} displays anomalous redshift until p_2, and a new peak appears abruptly at 171 cm^{-1} which increases to 181 cm^{-1} at 2.4 GPa. That this new split peak has the higher frequency indicates that two Ru atoms move close to each other and form a dimerized bond. By simply assuming that the distance of the nearest Ru atoms is inversely proportional with the frequency of the Ru in-plane mode, we can estimate that the Ru-Ru bond dimerization is about 0.5 Å at 2.4 GPa in agreement with previous XRD measurement [39].

The Ru-Ru dimerization in the α-$RuCl_3$ layers splits all degenerated E modes into $A + B$ modes. We do observe such a splitting for the twist mode at 116 cm^{-1} and the shearing mode at 268 cm^{-1} (it splits at p_1 probably is due to the interlayer interaction). We did not detect the splitting for the ring breathing mode at 294 cm^{-1}, probably due to its low intensity and the adjacent intensive 310-cm^{-1} mode. The two splitting peaks of the original 161-cm^{-1} mode at p_2 can be assigned as A_g for high-frequency mode and B_g for the low-frequency one, and the A_g peak becomes much more intense than the B_g peak with the increasing pressure as shown in Fig. 1. If using 488-nm laser as excitation light, the B_g peak even becomes unresolvable as shown in Fig. 7. Similarly, the B_g peak of the split 116-cm^{-1} mode has lower frequency and cannot be observed after the dimerization. For the 268-cm^{-1} mode after splitting, the B_g peak has higher frequency than A_g peak and disappears after the phase transition at p_2. All these observations on the Raman modes are consistent with the scenario of Ru-Ru bond dimerization.

C. Magnetic collapse from Raman susceptibility

Raman spectroscopy also detects the magnetic response in the strong spin-orbit coupling system [43,45–47]. The Raman intensity $I(\omega)$ is proportional to the dynamical Raman tensor susceptibility as $I(\omega) \propto [1 + n(\omega)]\chi''(\omega)$. Here, $\chi''(\omega)$ is the imaginary part of the correlation functions of Raman tensor $\tau(\mathbf{r}, t)$, $\chi(\omega) = \int_0^\infty dt \int d\mathbf{r}\langle\{\tau(0,0), \tau(\mathbf{r}, t)\}\rangle e^{-i\omega t}$. In general, the Raman tensor $\tau(\mathbf{r})$ can be expanded in powers of spin-1/2 operators, $\tau^{\alpha\beta}(\mathbf{r}) = \tau_0^{\alpha\beta}(\mathbf{r}) + \sum_\mu K_\mu^{\alpha\beta} S^\mu(\mathbf{r}) + \sum_\delta \sum_{\mu\nu} M_{\mu\nu}^{\alpha\beta}(\mathbf{r}, \delta) S_{\mathbf{r}}^\mu S_{\mathbf{r}+\delta}^\nu + \ldots$. The first term corresponds to Rayleigh scattering, the second and third terms correspond to the one spin flip [43,45,46] and two spin flip process [43,45–48,51], respectively. The complex tensors K and M are the coupling strength of light to the spin system.

To extract the magnetic Raman susceptibility, we integrate the Raman conductivity [see Fig. 5(a), the phonon peaks are subtracted from the original Raman spectra] over the frequency range from 15 to 220 cm^{-1} according to the Kramers-Kronig relation $\chi_R \equiv \frac{2}{\pi} \int \frac{\chi''(\omega)}{\omega} d\omega$. The results are plotted in Fig. 5(b) where the pressure dependence of χ_R manifests a rapid increase, slightly adjusted at p_1, then followed by a sharp drop towards zero at p_2. The Raman susceptibility χ_R contains the one-spin susceptibility and multiple-spin susceptibility (e.g., two-spin bond correlation), corresponding to one-spin flip and multi-spin flip processes, respectively. Since the static spin susceptibility χ_m of α-$RuCl_3$ at room temperatures changes little before dimerization as reported in Refs. [38,40], the rapid increasing Raman susceptibility χ_R

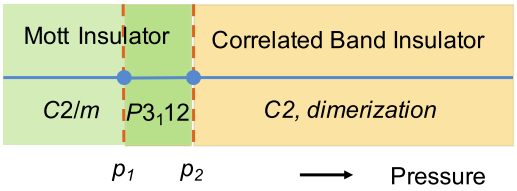

FIG. 6. Schematic phase diagram of α-$RuCl_3$ under pressures. The crystal structure changes from $C2/m$ to $P3_112$ at p_1 signaled by inversion symmetry breaking, and further to $C2$ at p_2 due to the Ru-Ru bond dimerization. For $p < p_2$, the system is a Mott insulator; after the bond dimerization for $p > p_2$, it becomes a correlated band insulator with Mott collapse.

should mainly come from the multispin flip processes. Beyond p_2, the Raman susceptibility χ_R tends to vanish, consistent with the dimerized nonmagnetic scenario.

Furthermore, as shown in Fig. 5(c), the Raman spectra of the phonon modes at 116 and 161 cm^{-1} display a significant Fano asymmetry for $p < p_2$ due to the couplings between the lattice and magnetic excitations. The coupling strength is measured by the full width at half maximum (FWHM) and the Fano asymmetry parameter $1/|q|$, as shown in Fig. 5(d), where we observe that the coupling strength increases with pressure and is completely suppressed after dimerization, consistent with the evolution of Raman susceptibility χ_R in Fig. 5(b).

V. DISCUSSIONS AND CONCLUSIONS

According to the previous studies, α-$RuCl_3$ has a monoclinic $C2/m$ structure at room temperature at ambient pressure and undergoes a stacking order phase transition when temperature is decreasing. From the recent high pressure studies, increasing pressure has similar effect on the material as decreasing temperature. We believe that the stacking order phase transition observed at $p_1 = 1.1$ GPa is the same one as obtained by decreasing temperature. However, in previous literature, three low temperature structures have been reported: the monoclinic $C2/m$, the trigonal $P3_112$, and the rhombohedral R-3 [56]. To pick up a reasonable structure out of three, we need to invoke our Raman and SHG data, which give clear evidence of the inversion symmetry breaking at this transition. Therefore it is very possible that the structure is changed from $C2/m$ to $P3_112$, with the inversion symmetry breaking, since the other two low temperature structures still possess the inversion symmetry. Our analysis is consistent with the XRD result recently reported by Wang [37].

The structural transition at p_1 is of first-order as indicated by the dramatic changes of FWHM and $1/|q|$ in Fig. 5(d). At $p_2 = 1.7$ GPa, the softening and big splitting of the Ru in-plane mode provide direct evidence of dimerization. Note that such a softening is not complete, therefore the dimerization transition at p_2 is also a first-order one according to the "little phonon softening" theory [57]. Such a dimerization leads to the Mott collapse, and the system becomes a band insulator with space group C_2. The schematic phase diagram is summarized in Fig. 6.

More remarks on the Mott collapse are needed here. The spin-orbit coupling splits the degenerate t_{2g} bands of α-$RuCl_3$ into the effective $j_{\text{eff}} = 1/2$ and $3/2$ bands. The former one is near the Fermi level with a narrower bandwidth comparing to the original t_{2g} band, such that the onsite Coulomb interaction U can turn the system into a Mott insulator at ambient pressure. However, the splitting between the effective $j_{\text{eff}} = 1/2$ and $3/2$ bands is not large enough, such that a moderate pressure could increase the bandwidth and bring the system close to the Mott transition, until finally drive the system into a nonmagnetic band insulator. The Ru-Ru bond dimerization accelerates this Mott collapse process. According to the first-principles calculations, this nonmagnetic state is a correlation-induced insulating phase, dubbed as the correlated band insulator [58]. The magnetic collapse is also confirmed by recent first-principles simulations in the dimmerized structure [39,40]. Magnetism and chemical bondings have also been studied in the isostructural counterpart α-$MoCl_3$ by the Raman scattering [59]. The spin-orbit coupling and Mott physics make the relativity and correlation effects more significant in the studies of magnetism and chemical bonds [1].

In conclusion, we perform Raman studies on the relation between Kitaev magnetism and chemical bondings in α-$RuCl_3$ under pressures. There are two critical pressures at $p_1 = 1.1$ GPa and $p_2 = 1.7$ GPa. At p_1, the α-$RuCl_3$ undergoes a structural transition with the inversion symmetry breaking due to different layer stacking, and the system remains a Mott insulator though the space group changes from the monoclinic $C2/m$ to the trigonal $P3_112$. At p_2, the Ru-Ru bonds dimerize and the system becomes a correlated band insulator through the Mott transition. Both transitions are of first order.

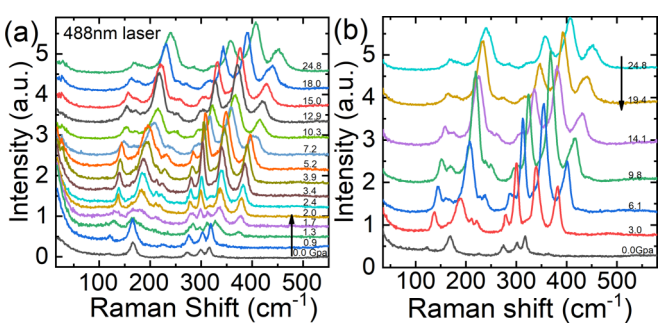

FIG. 7. Evolution of Raman spectrum of α-$RuCl_3$ with increasing pressure (a) and decreasing pressure(b) excited by 488-nm laser.

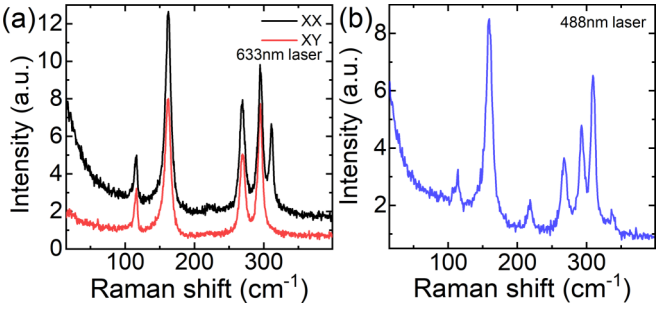

FIG. 8. (a) Raman spectra measured in (XX) and (XY) polarization for α-$RuCl_3$ by a 633-nm laser at ambient pressure. (b) The Raman spectrum of α-$RuCl_3$ by a 488-nm laser at ambient pressure.

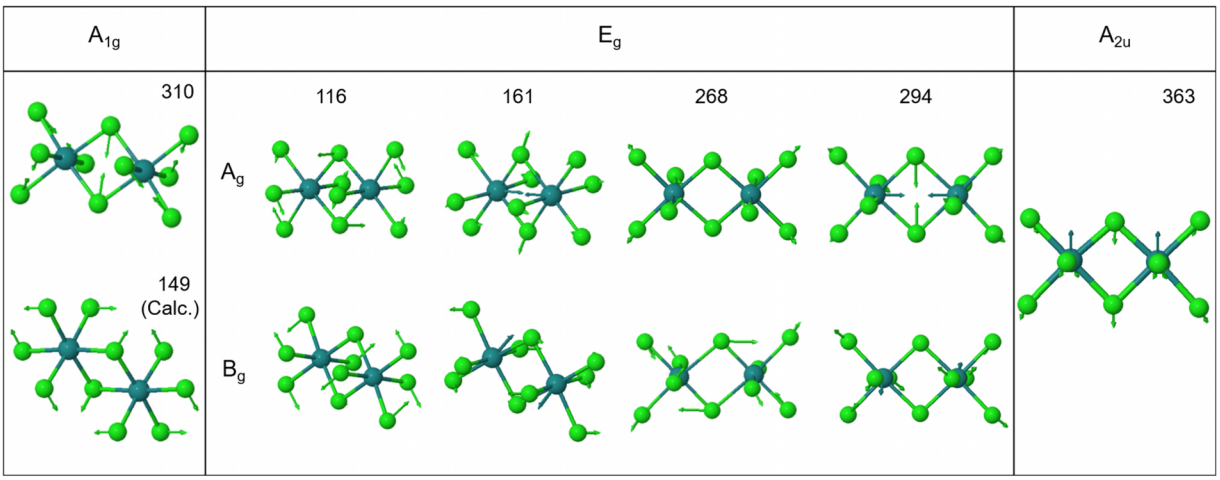

FIG. 9. The atomic displacement of the Raman active modes along with the IR-active asymmetrical layer breathing modes (the frequency unit is cm^{-1}).

ACKNOWLEDGMENTS

We would like to thank Hugen Yan for the IR measurement on the exfoliated α-$RuCl_3$ layers and Shunhong Zhang for useful discussions at the early stage of this work. This work was supported by the Science, Technology and Innovation Commission of Shenzhen Municipality (Grant No. ZDSYS20170303165926217). M.H. was partially supported by the Science, Technology and Innovation Commission of Shenzhen Municipality (Grant Nos. JCYJ20170412152334605 and JCYJ20160531190446212). F.Y. was partially supported by National Natural Science Foundation of China (Grant No. 11774143) and the Science, Technology and Innovation Commission of Shenzhen Municipality (Grant No. JCYJ20160531190535310). J.W.M was partially supported by the program for Guangdong Introducing Innovative and Entrepreneurial Teams (No. 2017ZT07C062)

APPENDIX A: PRESSURE DEPENDENT RAMAN SPECTRUM OF α-$RuCl_3$ EXCITED BY 488-nm LASER

The evolution of the Raman spectrum of α-$RuCl_3$ with increasing pressure excited by a 488-nm laser is displayed in Fig. 7(a). The main feature of this pressure-dependent Raman spectrum is the same with that excited by a 633-nm laser as shown in Fig. 1. Three new Raman modes at about 201, 290, and 363 cm^{-1} appear at around 1.1 GPa and peak splittings or a frequency jumping are observed at 1.7 GPa for the modes at 116, 161, and 268 cm^{-1}. The main difference is that the original peak of the Ru in-plane mode (161 cm^{-1}) is unresolvable after 1.7 GPa and the mode at 294 cm^{-1} becomes weaker and unresolvable at high pressure. The difference might come from the Raman scattering cross section changes with excitation laser and the lower resolution due to the short wavelength. After 1.7 GPa, no sudden change is observed in the spectrum. In addition, the evolution of the Raman spectrum of α-$RuCl_3$ with the decreasing pressure is shown in Fig. 7(b). The Raman spectrum can return to the original state with decreasing pressure from 24.8 to 0 GPa, which means this process is reversible.

APPENDIX B: POLARIZED RAMAN SPECTRUM OF α-$RuCl_3$

The Raman spectra were measured in both parallel (XX) and crossed (XY) polarizations with a polarized 633-nm laser. The polarized Raman spectra of α-$RuCl_3$ are shown in Fig. 8(a). The first four modes are present in both polarization channels and therefore assigned as a doubly degenerated E_g mode. The last mode at 310 cm^{-1} is suppressed in the crossed (XY) geometry and so can be assigned as A_{1g} symmetry, which is consistent with the previous Raman studies [52]. In addition, the Raman spectrum of α-$RuCl_3$ was also measured by a 488-nm laser at ambient pressure. From Fig. 8(b), there are two new weak peaks at 218 and 339 cm^{-1}. Considering the weak intensity and our first-principles calculation, we believe the two new peaks come from defect modes.

APPENDIX C: THE ATOMIC DISPLACEMENT OF THE RAMAN ACTIVE MODES OF α-$RuCl_3$

The calculated atomic displacements for the Raman active E_g modes are displayed in Fig. 9. There are two eigenvectors (one with A symmetry and the other with B symmetry) for each E_g mode. The Ru-Ru bond dimerization in the α-$RuCl_3$ layers splits all degenerated E modes, so the A and B modes will have different frequencies. Obviously, the twisting, shearing and breathing of the dimerized Ru-Cl-Ru-Cl ring will have higher frequencies, the same with the Ru in-plane modes along the dimerized direction. In short, the A mode will have higher frequencies for the twisting mode at 116 cm^{-1}, the Ru in-plane mode at 161 cm^{-1} and the ring breathing mode at 294 cm^{-1}, but it is opposite for the shearing mode at 268 cm^{-1}. We observed that all of the A modes have higher intensity after the dimerization and the B modes disappear or have lower intensity.

[1] J. B. Goodenough, *Magnetism and Chemical Bond*, Interscience Monographs on Chemistry: Inorganic Chemistry Section Vol. 1 (Interscience Publ., New York, 1963).

[2] I. Dzyaloshinsky, A thermodynamic theory of weak ferromagnetism of antiferromagnetics, J. Phys. Chem. Solids **4**, 241 (1958).

[3] T. Moriya, Anisotropic superexchange interaction and weak ferromagnetism, Phys. Rev. **120**, 91 (1960).

[4] L. Shekhtman, O. Entin-Wohlman, and A. Aharony, Moriya's Anisotropic Superexchange Interaction, Frustration, and Dzyaloshinsky's Weak Ferromagnetism, Phys. Rev. Lett. **69**, 836 (1992).

[5] D. Pesin and L. Balents, Mott physics and band topology in materials with strong spin-orbit interaction, Nat. Phys. **6**, 376 (2010).

[6] A. Kitaev, Anyons in an exactly solved model and beyond, Ann. Phys. **321**, 2 (2006).

[7] G. Jackeli and G. Khaliullin, Mott Insulators in the Strong Spin-Orbit Coupling Limit: From Heisenberg to a Quantum Compass and Kitaev Models, Phys. Rev. Lett. **102**, 017205 (2009).

[8] J. Chaloupka, G. Jackeli, and G. Khaliullin, Kitaev-Heisenberg Model on a Honeycomb Lattice: Possible Exotic Phases in Iridium Oxides A_2IrO_3, Phys. Rev. Lett. **105**, 027204 (2010).

[9] P. W. Anderson, The resonating valence bond state in La_2CuO_4 and superconductivity, Science **235**, 1196 (1987).

[10] X. G. Wen, *Quantum Field Theory of Many-Body Systems:From the Origin of Sound to an Origin of Light and Electrons*, Oxford Graduate Texts (OUP, Oxford, 2004).

[11] M. Levin and X.-G. Wen, Detecting Topological Order in a Ground State Wave Function, Phys. Rev. Lett. **96**, 110405 (2006).

[12] R. B. Laughlin, Anomalous Quantum Hall Effect: An Incompressible Quantum Fluid with Fractionally Charged Excitations, Phys. Rev. Lett. **50**, 1395 (1983).

[13] S. A. Kivelson, D. S. Rokhsar, and J. P. Sethna, Topology of the resonating valence-bond state: Solitons and high-T_c superconductivity, Phys. Rev. B **35**, 8865 (1987).

[14] N. Read and B. Chakraborty, Statistics of the excitations of the resonating-valence-bond state, Phys. Rev. B **40**, 7133 (1989).

[15] N. Read and S. Sachdev, Large-N Expansion for Frustrated Quantum Antiferromagnets, Phys. Rev. Lett. **66**, 1773 (1991).

[16] X. G. Wen, Mean-field theory of spin-liquid states with finite energy gap and topological orders, Phys. Rev. B **44**, 2664 (1991).

[17] F. Ye, P. A. Marchetti, Z. B. Su, and L. Yu, Hall effect, edge states, and Haldane exclusion statistics in two-dimensional space, Phys. Rev. B **92**, 235151 (2015).

[18] F. Ye, P. A. Marchetti, Z. B. Su, and L. Yu, Fractional exclusion and braid statistics in one dimension: a study via dimensional reduction of Chern-Simons theory, J. Phys. A: Math. Theor. **50**, 395401 (2017).

[19] S. K. Choi, R. Coldea, A. N. Kolmogorov, T. Lancaster, I. I. Mazin, S. J. Blundell, P. G. Radaelli, Y. Singh, P. Gegenwart, K. R. Choi, S.-W. Cheong, P. J. Baker, C. Stock, and J. Taylor, Spin Waves and Revised Crystal Structure of Honeycomb Iridate Na_2IrO_3, Phys. Rev. Lett. **108**, 127204 (2012).

[20] Y. Singh, S. Manni, J. Reuther, T. Berlijn, R. Thomale, W. Ku, S. Trebst, and P. Gegenwart, Relevance of the Heisenberg-Kitaev Model for the Honeycomb Lattice Iridates A_2IrO_3, Phys. Rev. Lett. **108**, 127203 (2012).

[21] S. H. Chun, J.-W. Kim, J. Kim, H. Zheng, C. C. Stoumpos, C. D. Malliakas, J. F. Mitchell, K. Mehlawat, Y. Singh, Y. Choi, T. Gog, A. Al-Zein, M. M. Sala, M. Krisch, J. Chaloupka, G. Jackeli, G. Khaliullin, and B. J. Kim, Direct evidence for dominant bond-directional interactions in a honeycomb lattice iridate Na_2IrO_3, Nat. Phys. **11**, 462 (2015).

[22] K. W. Plumb, J. P. Clancy, L. J. Sandilands, V. V. Shankar, Y. F. Hu, K. S. Burch, H.-Y. Kee, and Y.-J. Kim, α-$RuCl_3$: A spin-orbit assisted Mott insulator on a honeycomb lattice, Phys. Rev. B **90**, 041112(R) (2014).

[23] R. D. Johnson, S. C. Williams, A. A. Haghighirad, J. Singleton, V. Zapf, P. Manuel, I. I. Mazin, Y. Li, H. O. Jeschke, R. Valentí, and R. Coldea, Monoclinic crystal structure of α-$RuCl_3$ and the zigzag antiferromagnetic ground state, Phys. Rev. B **92**, 235119 (2015).

[24] J. A. Sears, M. Songvilay, K. W. Plumb, J. P. Clancy, Y. Qiu, Y. Zhao, D. Parshall, and Young-June Kim, Magnetic order in α-$RuCl_3$: A honeycomb-lattice quantum magnet with strong spin-orbit coupling, Phys. Rev. B **91**, 144420 (2015).

[25] A. Banerjee, C. A. Bridges, J.-Q. Yan, A. A. Aczel, L. Li, M. B. Stone, G. E. Granroth, M. D. Lumsden, Y. Yiu, J. Knolle, S. Bhattacharjee, D. L. Kovrizhin, R. Moessner, D. A. Tennant, D. G. Mandrus, and S. E. Nagler, Proximate Kitaev quantum spin liquid behavior in a honeycomb magnet, Nat. Mater. **15**, 733 (2016).

[26] S. C. Williams, R. D. Johnson, F. Freund, S. Choi, A. Jesche, I. Kimchi, S. Manni, A. Bombardi, P. Manuel, P. Gegenwart, and R. Coldea, Incommensurate counterrotating magnetic order stabilized by Kitaev interactions in the layered honeycomb α-Li_2IrO_3, Phys. Rev. B **93**, 195158 (2016).

[27] K. Ran, J. Wang, W. Wang, Z.-Y. Dong, X. Ren, S. Bao, S. Li, Z. Ma, Y. Gan, Y. Zhang, J. T. Park, G. Deng, S. Danilkin, S.-L. Yu, J.-X. Li, and J. Wen, Spin-Wave Excitations Evidencing the Kitaev Interaction in Single Crystalline α-$RuCl_3$, Phys. Rev. Lett. **118**, 107203 (2017).

[28] J. Zheng, K. Ran, T. Li, J. Wang, P. Wang, B. Liu, Z.-X. Liu, B. Normand, J. Wen, and W. Yu, Gapless Spin Excitations in the Field-Induced Quantum Spin Liquid Phase of α-$RuCl_3$, Phys. Rev. Lett. **119**, 227208 (2017).

[29] Y. J. Yu, Y. Xu, K. J. Ran, J. M. Ni, Y. Y. Huang, J. H. Wang, J. S. Wen, and S. Y. Li, Ultralow-Temperature Thermal Conductivity of the Kitaev Honeycomb Magnet α-$RuCl_3$ across the Field-Induced Phase Transition, Phys. Rev. Lett. **120**, 067202 (2018).

[30] N. Janša, A. Zorko, M. Gomilšek, M. Pregelj, K. W. Krämer, D. Biner, A. Biffin, C. Rüegg, and M. Klanjšek, Observation of two types of fractional excitation in the Kitaev honeycomb magnet, Nat. Phys. **14**, 786 (2018).

[31] S.-H. Baek, S.-H. Do, K.-Y. Choi, Y. S. Kwon, A. U. B. Wolter, S. Nishimoto, J. van den Brink, and B. Büchner, Evidence for a Field-Induced Quantum Spin Liquid in α-$RuCl_3$, Phys. Rev. Lett. **119**, 037201 (2017).

[32] A. Banerjee, P. Lampen-Kelley, J. Knolle, C. Balz, A. A. Aczel, B. Winn, Y. Liu, D. Pajerowski, J. Yan, C. A. Bridges, A. T. Savici, B. C. Chakoumakos, M. D. Lumsden, D. A. Tennant, R. Moessner, D. G. Mandrus, and S. E. Nagler, Excitations in the field-induced quantum spin liquid state of α-$RuCl_3$, npj Quantum Mater. **3**, 8 (2018).

[33] A. U. B. Wolter, L. T. Corredor, L. Janssen, K. Nenkov, S. Schönecker, S.-H. Do, K.-Y. Choi, R. Albrecht, J. Hunger,

T. Doert, M. Vojta, and B. Büchner, Field-induced quantum criticality in the Kitaev system α-$RuCl_3$, Phys. Rev. B **96**, 041405 (2017).

[34] Z. Wang, S. Reschke, D. Hüvonen, S.-H. Do, K.-Y. Choi, M. Gensch, U. Nagel, T. Rõom, and A. Loidl, Magnetic Excitations and Continuum of a Possibly Field-Induced Quantum Spin Liquid in α-$RuCl_3$, Phys. Rev. Lett. **119**, 227202 (2017).

[35] R. Hentrich, A. U. B. Wolter, X. Zotos, W. Brenig, D. Nowak, A. Isaeva, T. Doert, A. Banerjee, P. Lampen-Kelley, D. G. Mandrus, S. E. Nagler, J. Sears, Y.-J. Kim, B. Büchner, and C. Hess, Unusual Phonon Heat Transport in α-$RuCl_3$: Strong Spin-Phonon Scattering and Field-Induced Spin Gap, Phys. Rev. Lett. **120**, 117204 (2018).

[36] Y. Kasahara, T. Ohnishi, Y. Mizukami, O. Tanaka, S. Ma, K. Sugii, N. Kurita, H. Tanaka, J. Nasu, Y. Motome, T. Shibauchi, and Y. Matsuda, Majorana quantization and half-integer thermal quantum Hall effect in a Kitaev spin liquid, Nature (London) **559**, 227 (2018).

[37] Z. Wang, J. Guo, F. F. Tafti, A. Hegg, S. Sen, V. A. Sidorov, L. Wang, S. Cai, W. Yi, Y. Zhou, H. Wang, S. Zhang, K. Yang, A. Li, X. Li, Y. Li, J. Liu, Y. Shi, W. Ku, Q. Wu, R. J. Cava, and L. Sun, Pressure-induced melting of magnetic order and emergence of a new quantum state in α-$RuCl_3$, Phys. Rev. B **97**, 245149 (2018).

[38] Y. Cui, J. Zheng, K. Ran, J. Wen, Z.-X. Liu, B. Liu, W. Guo, and W. Yu, High-pressure magnetization and NMR studies of α-$RuCl_3$, Phys. Rev. B **96**, 205147 (2017).

[39] G. Bastien, G. Garbarino, R. Yadav, F. J. Martinez-Casado, R. B. Rodríguez, Q. Stahl, M. Kusch, S. P. Limandri, R. Ray, P. Lampen-Kelley, D. G. Mandrus, S. E. Nagler, M. Roslova, A. Isaeva, T. Doert, L. Hozoi, A. U. B. Wolter, B. Büchner, J. Geck, and J. van den Brink, Pressure-induced dimerization and valence bond crystal formation in the Kitaev-Heisenberg magnet α-$RuCl_3$, Phys. Rev. B **97**, 241108 (2018).

[40] T. Biesner, S. Biswas, W. Li, Y. Saito, A. Pustogow, M. Altmeyer, A. U. B. Wolter, B. Büchner, M. Roslova, T. Doert, S. M. Winter, R. Valentí, and M. Dressel, Detuning the honeycomb of α-$RuCl_3$: Pressure-dependent optical studies reveal broken symmetry, Phys. Rev. B **97**, 220401 (2018).

[41] V. Hermann, M. Altmeyer, J. Ebad-Allah, F. Freund, A. Jesche, A. A. Tsirlin, M. Hanfland, P. Gegenwart, I. I. Mazin, D. I. Khomskii, R. Valentí, and C. A. Kuntscher, Competition between spin-orbit coupling, magnetism, and dimerization in the honeycomb iridates: α-Li_2IrO_3 under pressure, Phys. Rev. B **97**, 020104 (2018).

[42] M. Majumder, R. S. Manna, G. Simutis, J. C. Orain, T. Dey, F. Freund, A. Jesche, R. Khasanov, P. K. Biswas, E. Bykova, N. Dubrovinskaia, L. S. Dubrovinsky, R. Yadav, L. Hozoi, S. Nishimoto, A. A. Tsirlin, and P. Gegenwart, Breakdown of Magnetic Order in the Pressurized Kitaev Iridate β-Li_2IrO_3, Phys. Rev. Lett. **120**, 237202 (2018).

[43] P. Lemmens, G. Güntherodt, and C. Gros, Magnetic light scattering in low-dimensional quantum spin systems, Phys. Rep. **375**, 1 (2003).

[44] T. P. Devereaux and R. Hackl, Inelastic light scattering from correlated electrons, Rev. Mod. Phys. **79**, 175 (2007).

[45] T. Moriya, Theory of absorption and scattering of light by magnetic crystals, J. Appl. Phys. **39**, 1042 (1968).

[46] P. A. Fleury and R. Loudon, Scattering of light by one- and two-magnon excitations, Phys. Rev. **166**, 514 (1968).

[47] J. Nasu, J. Knolle, D. L. Kovrizhin, Y. Motome, and R. Moessner, Fermionic response from fractionalization in an insulating two-dimensional magnet, Nat. Phys. **12**, 912 (2016).

[48] J. Fu, J. G. Rau, M. J. P. Gingras, and N. B. Perkins, Fingerprints of quantum spin ice in Raman scattering, Phys. Rev. B **96**, 035136 (2017).

[49] B. S. Shastry and B. I. Shraiman, Theory of Raman Scattering in Mott-Hubbard Systems, Phys. Rev. Lett. **65**, 1068 (1990).

[50] W.-H. Ko, Z.-X. Liu, T.-K. Ng, and P. A. Lee, Raman signature of the U(1) Dirac spin-liquid state in the spin-$\frac{1}{2}$ kagome system, Phys. Rev. B **81**, 024414 (2010).

[51] J. Knolle, G.-W. Chern, D. L. Kovrizhin, R. Moessner, and N. B. Perkins, Raman Scattering Signatures of Kitaev Spin Liquids in A_2IrO_3 Iridates with A = Na or Li, Phys. Rev. Lett. **113**, 187201 (2014).

[52] L. J. Sandilands, Y. Tian, K. W. Plumb, Y.-J. Kim, and K. S. Burch, Scattering Continuum and Possible Fractionalized Excitations in α-$RuCl_3$, Phys. Rev. Lett. **114**, 147201 (2015).

[53] A. Glamazda, P. Lemmens, S. H. Do, Y. S. Choi, and K. Y. Choi, Raman spectroscopic signature of fractionalized excitations in the harmonic-honeycomb iridates β- and γ-Li_2IrO_3, Nat. Commun. **7**, 12286 (2016).

[54] A. Glamazda, P. Lemmens, S.-H. Do, Y. S. Kwon, and K.-Y. Choi, Relation between Kitaev magnetism and structure in α-$RuCl_3$, Phys. Rev. B **95**, 174429 (2017).

[55] N. Caswell and S. A. Solin, Vibrational excitations of pure $FeCl_3$ and graphite intercalated with ferric chloride, Solid State Commun. **27**, 961 (1978).

[56] Y. Hasegawa, T. Aoyama, K. Sasaki, Y. Ikemoto, T. Moriwaki, T. Shirakura, R. Saito, Y. Imai, and K. Ohgushi, Two-phonon absorption spectra in the layered honeycomb compound α-$RuCl_3$, J. Phys. Soc. Jpn. **86**, 123709 (2017).

[57] J. A. Krumhansl and R. J. Gooding, Structural phase transitions with little phonon softening and first-order character, Phys. Rev. B **39**, 3047 (1989).

[58] H.-S. Kim, V. Shankar, V. A. Catuneanu, and H.-Y. Kee, Kitaev magnetism in honeycomb $RuCl_3$ with intermediate spin-orbit coupling, Phys. Rev. B **91**, 241110 (2015).

[59] M. A. McGuire, J. Yan, P. Lampen-Kelley, A. F. May, V. R. Cooper, L. Lindsay, A. Puretzky, L. Liang, Santosh KC, E. Cakmak, S. Calder, and B. C. Sales, High-temperature magnetostructural transition in van der Waals-layered α-$MoCl_3$, Phys. Rev. Mater. **1**, 064001 (2017).